Influence of anneal atmosphere on ZnO-nanorod photoluminescent and morphological properties with self-powered photodetector performance

Hatch, SM; Briscoe, J; Sapelkin, A; Gillin, WP; Gilchrist, JB; Ryan, MP; Heutz, S; Dunn, S

For additional information about this publication click this link.
http://qmro.qmul.ac.uk/jspui/handle/123456789/6292

Influence of anneal atmosphere on ZnO-nanorod photoluminescent and morphological properties with self-powered photodetector performance

S. M. Hatch, J. Briscoe, A. Sapelkin, W. P. Gillin, J. B. Gilchrist, M. P. Ryan, S. Heutz, and S. Dunn

Influence of anneal atmosphere on ZnO-nanorod photoluminescent and morphological properties with self-powered photodetector performance

S. M. Hatch,[1] J. Briscoe,[1] A. Sapelkin,[2] W. P. Gillin,[2] J. B. Gilchrist,[3] M. P. Ryan,[3] S. Heutz,[3] and S. Dunn[1,a)]

[1]*School of Engineering and Material Science, Queen Mary University of London, Mile End Road, London E1 4NS, United Kingdom*
[2]*School of Physics and Astronomy, Queen Mary University of London, Mile End Road, London E1 4NS, United Kingdom*
[3]*Department of Materials, Imperial College London, South Kensington Campus, London SW7 2AZ, United Kingdom*

ZnO nanorods synthesised using an aqueous pH 11 solution are shown to exhibit surface-sensitive morphology post-annealing in oxygen, air, and nitrogen as shown by scanning electron microscopy and transmission electron microscopy analysis. Raman analysis confirms the nanorods were nitrogen-doped and that nitrogen incorporation takes place during the synthesis procedure in the form of N-H_x. A strong green photoluminescence is observed post-annealing for all samples, the intensity of which is dependent on the atmosphere of anneal. This luminescence is linked to zinc vacancies as recent reports have indicated that these defects are energetically favoured with the annealing conditions used herein. ZnO-nanorod/CuSCN diodes are fabricated to examine the effect of material properties on photodetector device performance. The devices exhibit a photocurrent at zero bias, creating a self-powered photodetector. A photocurrent response of 30 μA (at 6 mW cm^{-2} irradiance) is measured, with a rise time of $\sim$25 ns, and sensitivity to both UV and visible light (475–525 nm). © 2013 AIP Publishing LLC. [http://dx.doi.org/10.1063/1.4805349]

I. INTRODUCTION

ZnO is a metal-oxide semiconductor with a wide band gap ($\sim$3.3 eV), high exciton binding energy ($\sim$60 meV), chemical stability, radiation hardness, photoconductivity and piezoelectric properties. These properties, as well as the relative ease with which ZnO nanostructures can be grown, lend themselves to use in nanoscale field effect transistors,[1] anti-reflection coatings,[2] energy-harvesting,[3–5] and optoelectronic[6,7] devices.

ZnO nanorods can be synthesised at low-temperatures (<100 °C) using aqueous chemical growth from a variety of chemical precursor mixtures such as zinc nitrate hexahydrate ($Zn(NO)_3 \cdot 6H_2O$) and hexamethylenetetramine (HMT).[8] This low-temperature process is advantageous for depositing on flexible polymer substrates and offers inexpensive processing suitable for mass-production. Numerous studies have demonstrated the sensitivity of this process to pH, precursor concentration, temperature, duration, pressure, and capping agents.[8–10] Even though the process developed by Vayssieres[11] is well-established, numerous variations of this growth method exist due to the number of growth parameters. Furthermore, these studies typically focus on the materials analysis and rarely demonstrate the effect on the overall device behavior. It is important to improve our understanding of how the synthesis process not only affects the characteristics of the material but also the overall device performance.

The aqueous growth method relies upon the preferential adsorption of Zn-precursors to the positive polar face (0001) before they dehydrate and enter the crystal lattice. As the non-polar faces of the wurtzite structure have a significantly lower surface energy than the positive (0001) plane, this gives rise to the anisotropic growth of ZnO in the c-axis direction. Rapid preferential growth on (0001) plane is indicated by tapering of the edges and the formation of needle-like tips;[12] furthermore, this plane also dissolves fastest under reverse equilibrium, forming ZnO nanotubes.[13,14]

The low-temperature and pressure environment of aqueous growth gives rise to native defects forming in the ZnO lattice due to their low formation energies and stability at these temperatures.[15,16] Point and structural defects in the ZnO lattice strongly influence the morphological, optical, and electrical properties of ZnO as-produced material. Hydrogen impurities have been associated with the n-type conductivity typically exhibited by ZnO.[17] Nitrogen-doping (N-doping) was reported to induce p-type conductivity through the implantation of acceptor-type defects.[18–20] However, studies have since shown that N-doping compensates p-type behaviour by forming shallow donors rather than acceptors, consequently p-type ZnO is unlikely to form.[21–25]

Point defects situated deep in the ZnO bandgap (E_g) give rise to photoluminescence (PL) referred to as deep-level emission (DLE) observed under excitation >E_g. This DLE emission has been employed in visible light-emitting diodes[26,27] and photodetectors.[28] However, the origins of DLE are far from certain; green emission (2.4–2.5 eV), in particular, has been debated extensively for over 30 yr;[29–32] red emission (1.5–2.0 eV) is often assigned to a number

---

a)Author to whom correspondence should be addressed. Electronic mail: s.c.dunn@qmul.ac.uk

of surface-related defects,[33] whereas yellow/orange (2.1–2.2 eV) emission is linked to oxygen interstitials[34,35] or extrinsic Li impurities.[16] Thermal annealing is often used to remove impurities and structural defects from the crystal lattice. However, depending on the anneal atmosphere, temperature, and duration new point defects can be introduced into the ZnO lattice.[32,36,37] These act as new emission centers or passivators that influence the PL emission.
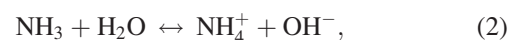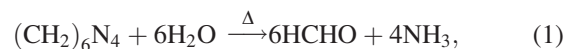
First-principle calculations determine the defect formation energies as a function of Fermi energy for specific environmental conditions. Coupled with the defect binding energies, first-principle calculations are often used to infer defect sources responsible for DLE. The importance of determining the emission source stems from the desire to manipulate optical, electrical, and morphological properties of ZnO to our advantage. Flexible electronic devices (e.g., piezoelectric energy-harvesting devices, solar cells, and light emitting diode (LED) displays) require low-temperature processing, which as discussed leads to unintentional doping and defect incorporation. It is, therefore, essential to understand the consequences low-temperature processing has on ZnO properties that govern device performance.

Self-powered photodetectors that operate entirely on the nanoscale (i.e., no external power supply) are becoming of increasing interest as shown by the growing number of recent articles.[28,38–41] These photodetectors often rely on the photovoltaic behavior to generate a photocurrent response at 0 V. The rise (τ_r) and fall (τ_f) response times (defined as the time required for the photocurrent to increase/decrease from 10% to 90%/90% to 10% of its maximum value, respectively) are important parameters when considering the photodetector effectiveness. A recent example reported by Deng *et al.*[42] used opposing heterostructures of p-type polyaniline nanowires sandwiched between two ZnO nanorod arrays. This produced a photocurrent response of 14 μA (to 8 W UV irradiance) after functionalising the nanorods with an absorbing polymer; however, no spectral sensitivity or response times were quoted for this device.

The photosensitivity of a photodetector is typically quoted as $(I_{photo} - I_{dark})/I_{dark}$. For photodetectors operating at an applied bias, this provides a ratio between current in the on and off states. However, with no applied bias no current is generated in the dark and so I_{dark} is zero. Therefore, for a self-powered photodetector where there is no applied bias this expression for photosensitivity cannot be used as it would always be infinite. Here, we use the maximum photocurrent at the lowest possible bias (Keithley 2400 set to 0 V) to indicate the photosensitivity. In principle, this gives the photocurrent at zero bias. However, a small bias is always present in the measurement system, as must be the case for previous self-powered photodetectors since non-zero dark currents are always measured.[15–18]

Here, we report the effect of materials processing on the ZnO properties and on the performance of nanorod-based photodetector devices using a highly alkaline (pH 11) solution consisting of HMT, zinc nitrate, and ammonia to synthesise the ZnO nanorods. In the ZnO synthesis, HMT is reported to act as a pH buffer that gradually decomposes to supply ammonia and hydroxyl ions to the reaction (Eqs. (1)

and (2)).[13,43,44] For ∼pH 11 solutions, production of ZnO occurs via the equilibrium reactions shown in Eqs. (3) and (4).[45] This indicates that once the Zn-precursors are exhausted, dissolution of ZnO will initiate. The chemical reactions for the aqueous synthesis at 90 °C are given as

$$(CH_2)_6N_4 + 6H_2O \xrightarrow{\Delta} 6HCHO + 4NH_3, \quad (1)$$

$$NH_3 + H_2O \leftrightarrow NH_4^+ + OH^-, \quad (2)$$

$$Zn(OH)_4^{2-} \leftrightarrow ZnO + H_2O + 2OH^-, \quad (3)$$

$$Zn(NH_3)_4^{2+} + 2OH^- \leftrightarrow ZnO + 4NH_3 + H_2O. \quad (4)$$

We show that this process produces N-doped ZnO nanorods that exhibit strong green (2.4 eV) emission post-annealing at 400 °C. Experimental characterisation using scanning electron microscopy (SEM), transmission electron microscopy (TEM), X-ray diffraction (XRD), Raman and photoluminescence spectroscopy, and previously reported theoretical calculations were used to infer green emission observed here is linked to zinc vacancies (V_{Zn}). To demonstrate the effect on device performance, four self-powered ZnO/CuSCN photodiodes were fabricated using N-doped ZnO nanorods as-grown, and annealed in air, nitrogen, or oxygen. The photodiodes show sensitivity to UV (360-400 nm) and visible (475-535 nm) wavelengths. A maximum photocurrent response of 30 μA (for 6 mW cm^{-2} UV irradiance) was measured at near zero-bias with a rise time of 25 ns and fall time of 4 ms.

II. EXPERIMENTAL SECTION

A. Device fabrication

A fluorine-doped tin oxide (FTO) coated glass substrate (15 Ω/square) was thoroughly cleaned using acetone followed by isopropanol for 15 min in an ultrasonic bath at room temperature (RT). A 0.005 M solution of zinc acetate dihydrate (Sigma Aldrich $\geq$ 98%) in absolute ethanol (purity > 99.7%) was deposited drop-wise on the FTO and annealed at 350 °C for 25 min. The process was repeated three times. A sealable glass vessel was used for the synthesis process, which prevented the evaporation of the solution. The seeded-substrates were then suspended FTO-face down in an aqueous solution consisting of: 15 ml of 0.2M zinc nitrate hexahydrate (Sigma Aldrich 99+%) solution (18 mM), 15 ml of 0.8 M HMT (Sigma Aldrich 98%) solution (73 mM), and 135 ml of 0.2 M ammonia hydroxide solution (0.163 M), which resulted in a final solution of pH 11. Synthesis solutions were made using de-ionised water with purity of ∼18 MΩ. The sealed vessel was placed in a (Town + Mercer EV018) pre-heated oven for 4 h at 90 °C $\pm$ 3 °C. The synthesis process was repeated eight times with fresh solution.

Nanorods were annealed using a tube furnace (Lenton Type 3216CC) that allowed selected gases to flow over the substrate surface at a rate of 1.0 l/min. The samples were heated to 400 °C and held for 60 min before unassisted cooling.

A 0.2 M CuSCN solution was made using 0.243 g of CuSCN (99% Sigma Aldrich) dissolved in 10.0 ml dipropyl sulfide (97% Sigma Aldrich). The solution was deposited on

a pre-heated ZnO-nanorod array (at 85 °C) using a spray-gun that produced an aerosol of CuSCN.[46] Finally, 0.1 cm^2 gold top electrodes were sputtered onto the CuSCN surface.

B. Characterisation

Morphological analysis was conducted using an FEI Inspect-F SEM operating at 20 kV and a JOEL 2010 F TEM (200 kV). TEM and selected area electron diffraction (SAED) patterns were performed on nanorods that had been scraped from the FTO into a vial of ethanol (GPR grade, VWR). This was sonicated for 5 min before depositing 1-2 drops of the suspension onto a Cu TEM grid. The XRD analysis was performed with an X'Pert PRO MPD θ-2θ System in θ-2θ Bragg-Brentano configuration with a diffracted beam monochromator. Grazing incidence XRD (GIXRD) was performed with a Siemens D500 using CuK$_\alpha$ radiation ($\lambda = 0.1540$ nm) under a glancing angle configuration of 3° with 2-D sample rotation. PL spectroscopy was performed at RT using a micro-Raman system in co-ordination with a He:Cd CW laser Triax 320 (325 nm excitation, 1200/1 mm grating, 30 mW output power). The samples characterized for PL and XRD were synthesised in the same solution to ensure continuity across data sets. Photo-voltage measurements were conducted using a Nd-YAG 532 nm pulsed laser with a 1 MΩ resistance connected in series with the device. The UV/vis absorption spectra were collected using a Perkin Elmer Lamba 950 spectrometer. Raman scattering measurements were performed using a Renishaw inVia monochromator equipped with CCD detector and a Nd-YAG 473 nm excitation source. The data for each sample were averaged over 30 acquisitions each with an exposure time of 10 s. Hall effect measurements were conducted via the Van der Pauw method. ZnO nanorods were grown onto clean 1 cm^2 square glass substrates. Four (right-angle triangle) gold contacts measuring 0.02 cm^2 were sputtered onto the ZnO in each corner. The sample was mounted onto a printed circuit board using silver paint. Hall mobility was calculated from an average of five measurements with the compliance voltage set to 5 V, a measuring current of 1.6 μA, and magnetic field of 0.5 T.

C. Electrical testing

Current-voltage (I-V) characteristics of the device were obtained via a Keithley 2400 with LABVIEW 8.2 software. The I-V sweep was conducted at room temperature under both dark and UV illumination. UV illumination consisted of a 380 nm wavelength LED positioned 1 cm directly above the sample with a measured intensity of 3.5 mW cm^{-2}. The output power for the 380 nm UV LED was measured using an International Light Technologies ILT14000-A Radiometer Photometer. Photocurrent measurements were conducted with the Keithley 2400 applied bias set to equal zero. The LEDs were sourced from RS Components (640 nm, 588 nm, 525 nm, and 470 nm) and Thorlabs (405 nm and 380 nm). The visible LEDs irradiances were measured and calibrated using an Ocean optics spectrometer. A range of intensities between 0.8 and 6.0 mW cm^{-2} were used to obtain the photocurrent measurements.

III. RESULTS AND DISCUSSION

A. ZnO synthesis and morphology

SEM analysis shows a densely populated array of ZnO nanorods 12–14 μm in length and 200–300 nm in diameter were formed after eight repeat syntheses in a pH 11 aqueous solution (Fig. 1). A wurtzite crystal structure and c-axis orientation of the nanorod array were confirmed for all samples by the prominent (002) XRD peak at 34.4° (JCPDS 36-1451, inset in Fig. 1(a)). Further SEM analysis post-annealing revealed a morphological sensitivity to the different atmospheres. Oxygen and air-annealed nanorods exhibit hexagonal columns with rounded tips and rough appearing surface (Fig. 1(b)). The nitrogen-annealed nanorods, however, possessed jagged, uneven peaks (Fig. 1(c)). GIXRD was performed to analyse the most recently formed portions in the nanorod tips, as it has a low penetration depth. It revealed significant crystallographic changes for different anneal-atmospheres. A dominant (103) peak orientation is shown for the nitrogen-annealed nanorods, see inset in Fig. 1(c). However, a significant rise in the (002) peak intensity is shown for increasing oxygen-anneal duration, see inset in Fig. 1(b).

Both the morphological and crystallographic analyses give evidence of transformations at the nanorod surface post-annealing. To determine the reason behind the differences, we employed the use of long-range Raman to analyse the nanorod surface, see Fig. 2(a) inset. We detected aliphatic carbon, N-H$_x$ species, and atmospheric nitrogen prior to annealing, which confirmed the presence of unreacted precursor material near the nanorod surface. Post-annealing these peaks are removed, which implies the anneal process has either removed or converted the precursor material.

The presence of unreacted precursors on the nanorod surface is assigned to the incomplete synthesis reaction and rapid nanorod growth in the c-axis direction as indicated by the tapered nanorod tips in Fig. 1(a). Consequently, this leads to unreacted precursors trapped at the nanorod surface after each subsequent 4 h synthesis in the pH 11 solution.

The difference in annealing behaviour is, therefore, assigned to the effect on the remnant Zn-precursors present on the nanorod surface post-synthesis. These precursors react with oxygen present during the oxygen/air-anneal process to form additional ZnO. The reducing nitrogen-anneal environment, however, inhibits additional ZnO growth and instead decomposes the remnant Zn-precursor material to form the surface observed in Fig. 1(c). TEM analysis further substantiates new crystal growth during the anneal process by the differences shown in the pre- and post-anneal SAED patterns. The well-defined wurtzite SAED pattern for as-grown nanorods (Fig. 2(b) inset) comes from a single crystal structure. However, the detection of multiple diffraction patterns post-annealing in air (Fig. 2(c) inset) indicates that new crystalline material has formed at different orientations to the original crystal.

The strong Raman E$_{2H}$ mode, dominant (002) XRD peak, and wurtzite TEM diffraction pattern data observed for all samples affirm the high ZnO crystallinity. The second-order Raman spectral peak (2-E$_{2M}$) at 329 cm^{-1}, the
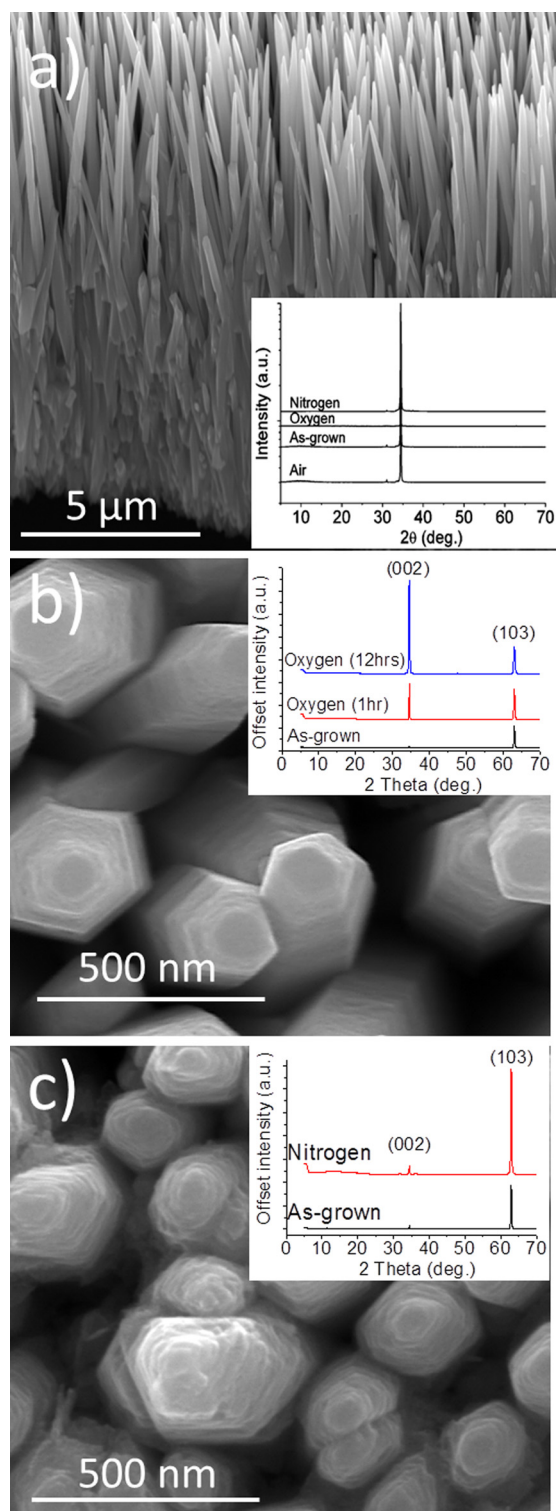
FIG. 1. SEM micrographs of ZnO nanorods showing (a) the cross-section of an as-grown nanorod array (tilted 45°) and XRD spectrum (inset), a top-down view of nanorods annealed in (b) oxygen and (c) nitrogen atmospheres with corresponding GIXRD spectrum (inset).
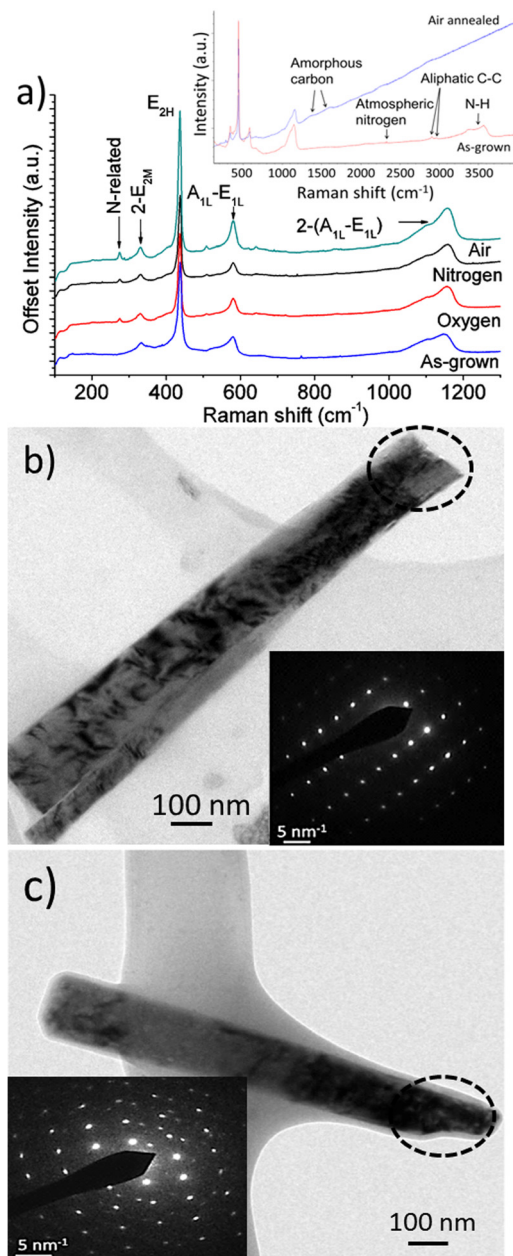

FIG. 2. (a) Raman spectra of ZnO nanorods post-processing with long-range Raman of air-annealed and as-grown ZnO nanorods (inset), TEM analysis of ZnO nanorods (b) as-grown and (c) air-annealed with corresponding SAED patterns inset.

first-order $(A_{1L}\text{-}E_{1L})$ mode at $579\,\text{cm}^{-1}$, and second-order $(2\text{-}(A_{1L}\text{-}E_{1L}))$ mode at $1158\,\text{cm}^{-1}$ are all associated with ZnO. Additional peaks at $273\,\text{cm}^{-1}$ and $508\,\text{cm}^{-1}$ were observed for annealed samples (Fig. 2(a)) and have previously been reported as nitrogen-related peaks.[47] The N-related peak is present for all annealed samples, which

implies the N-doping source originates from the synthesis process. This gives evidence that the N-H$_x$ species detected in long-range Raman analysis has not been completely removed but converted to form separate N-related species that resulted in the unintentional N-doping of the ZnO nanorods.

B. Electrical and optical properties

In order to give a guide whether acceptors or donors are the majority carriers in ZnO, Hall measurements were performed on the air-annealed sample. A bulk donor concentration of $n = 8.5 \times 10^{16}\,\text{cm}^{-3}$ confirmed ZnO was n-type, with a carrier mobility of $\mu_e = 1.63\,\text{cm}^2\,\text{V}\,\text{s}^{-1}$. Due to the

unconnected nature of the nanorods, only the bulk region of the ZnO array, consisting of fused nanorods at the base, was subject to the electric field. Hence, the thickness of this region ($\sim$4 μm—see Fig. 1(a)) was used to calculate the bulk concentration. The conductivity was calculated to be 1.2 S m^{-1}.

Visible observations of the ZnO nanorods showed a permanent colour change from the original cream-colour to pink, yellow, and brown post-annealing in air, oxygen, and nitrogen, respectively. ZnO is thermochromic; typically ZnO is grey at room temperature but becomes yellow when heated above 300 °C due to desorption of oxygen from the surface. Upon cooling, the re-adsorption of oxygen returns ZnO back to its original colour. The permanent colour change in ZnO has previously been assigned to the introduction of intrinsic defects during the anneal process.[48]

PL measurements were undertaken in order to probe the energy transitions within the ZnO and determine a relationship between material colour and defect structure. The normalised PL showed a low near band-edge emission (NBE) at $\sim$377 nm (3.3 eV) for all samples (Fig. 3). The highly crystalline ZnO as shown by XRD and Raman analysis would be expected to generate strong NBE. The diminished NBE indicates rapid recombination of charge carriers in the defect energy states, which gives rise to intense DLE observed in Fig. 3. The dependence of this DLE on the anneal atmosphere was analysed to investigate the defect structure. In order to compare the relative contributions to the DLE, Gaussian fits were made to the PL spectra.[63] The peak position, full-width half-maximum, and intensities derived from the Gaussian fits are given in Table I.

Yellow DLE at $\sim$565 nm (2.2 eV) was observed for the as-grown sample and has been previously been linked to Zn(OH)$_2$ on the surface.[33] However, in this case, the O-H stretching mode is overlapped by the N-H mode detected by Raman at 3200–3600 cm^{-1} so cannot be ascribed conclusively. Gaussian fits of the DLE[63] show that the 565 nm peak intensity is reduced in the air and nitrogen atmosphere but increases during the oxygen anneal. This agrees with the finding that O-H is a likely source for yellow emission.

Annealing of the ZnO nanorods resulted in the development of a broad green DLE peak at 504 nm (2.4 eV), with a
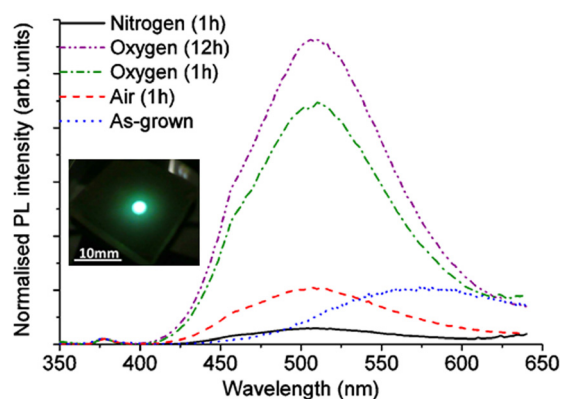

FIG. 3. Photoluminescence spectra of ZnO nanorods as-grown and post-annealed in oxygen, nitrogen, and air normalised to the exciton emission. Photograph inset is an example of the observed green emission.

shoulder in the blue region at $\sim$460 nm (2.7 eV), see Fig. 3. Blue emission at 460 nm was previously linked to the presence of zinc interstitials (Zn$_i$),[49] although numerous theoretical calculations show these defects are relatively unstable and would easily anneal out at 400 °C.[50–53] Look *et al.*,[54] however, proposed that complexes of Zn$_i$ and nitrogen impurities could be stable and act as shallow donors.

The peak fits show that the green (2.4 eV) emission was highest when annealed in oxygen, followed by air and nitrogen. The assignment of the green emission to a particular defect structure is a complex task, as a number of defects have previously been assigned to this emission.[29–31] Correlations between the green luminescence and oxygen vacancies (V$_O$) are frequently cited, which were based on V$_O$ being assigned to the g $\sim$1.96 line in EPR measurements.[55] This has since been shown to be due to shallow donors or conduction band electrons.[48] Furthermore, the V$_O$ electronic transition state (2+/0) is reported to be 0.5 eV (Ref. 53) or 0.4 eV (Ref. 52) above the valence band maximum (VBM) or 3.0 eV (Ref. 56) below the conduction band minimum (CBM), which makes V$_O$ an unlikely contributor to green emission. A growing body of evidence indicates that V$_{Zn}^{2-}$ may be a significant contributor to green luminescence. V$_{Zn}^{2-}$ has a transition between the (1$-$/2$-$) charge states 0.9 eV above the VBM. The transition from the conduction band to the ($-$1/$-$2) state would give rise to the green (2.4 eV) emission observed here. However, it must be considered whether it is possible to form V$_{Zn}$ using the synthesis and processing used here.

First-principle studies by Van de Walle *et al.* and numerous authors since[50–53] have used local-density-function approximations (LDA) to calculate the formation energies of various defects in ZnO. These latest studies are finding that V$_{Zn}^{2-}$ have the lowest formation energy in O-rich conditions for n-type ZnO. The high pH synthesis environment arises from the high quantity of available hydroxyl ions (see reaction schemes), which provides an excess of oxygen for the reaction. Hence, we propose that under the O-rich synthesis conditions, V$_{Zn}^{2-}$ are the most energetically favourable and stable defects to form in the ZnO-nanorods.

The absence of green emission prior to annealing is attributed to H$^+$ defects, which are present from various sources in the aqueous synthesis and considered to be shallow donors in ZnO. Van de Walle[57] suggested H-doping was the cause of ZnO n-type behaviour, and as a donor-defect it would effectively passivate acceptor-states such as V$_{Zn}^{2-}$.

Annealing the nanorods in any atmosphere crystallises the precursor material at the surface. Any N-H$_x$ on the surface is oxidised during the oxygen/air-anneal and ZnO is formed from the unreacted Zn-precursor material. Simultaneously, N-H$_x$ trapped in the nanorod bulk dissociates to form N- and H-related species. This leads to the N-doping of the nanorods, while the liberated H$^+$ gradually diffuses out of the nanorods or substitutes on available V$_O$ sites (H$_O$) forming shallow donors.[58] As a result, H$^+$ passivation of the V$_{Zn}^{2-}$ defects and associated PL quenching is significantly reduced.[59] Due to the nanorod morphology and low H$_2$ partial pressure of all anneal atmospheres, we predict the outward diffusion rate of H$_2$ to be similar for all

TABLE I. Peak position, full-width half-maximum, and intensity of DLE peaks contributing to the spectra shown in Fig. 3 obtained from Gaussian fits.[63]

	As-grown	Nitrogen (1 h)			Air (1 h)			Oxygen (1 h)			Oxygen (12 h)		
Peak position (nm)	565	458	504	565	458	504	565	458	504	565	458	504	565
FWHM (nm)	112	42	76	130	35	81	137	27	83	131	26	85	116
Intensity (normalised)	9.8	0.6	2.3	1.2	1.9	8.2	3.5	5.3	37.0	13.2	6.3	48.7	15.4

atmospheres; hence, the appearance of green DLE post-annealing in all cases.

To account for the dependence of green emission intensity on the anneal atmosphere, we propose two processes occur during the thermal anneal: first, the oxidation of remnant Zn-precursors to form new ZnO (oxygen/air-anneal only), and second, once the Zn-precursors are exhausted, newly formed ZnO at the nanorod surface is subject to the formation of additional V_{Zn}^{2-} under high oxygen partial pressure conditions (oxygen-anneal only). Neither of these processes occur during the reducing nitrogen-anneal. Instead, the Zn-precursors decompose forming an amorphous region at the surface that quenches emission from the bulk, or alternatively compensators (e.g., V_O, N_{Zn}, (N_{Zn}–$2V_{Zn}$), or (Zn_i-N_O)) are formed that passivate V_{Zn}^{2-} sites and quench the emission. This explains the observed trend of DLE intensity in Fig. 3: oxygen > air > nitrogen. The prolonged 12 h oxygen-anneal indicates that the defect responsible for the green emission is relatively stable at temperatures of ~400 °C (Fig. 3).

Tam *et al.*[31] used positron annihilation spectroscopy (PAS) to link acceptor-like V_{Zn} defects to the green emission. It was pointed out that single-point defects are relatively mobile at high temperatures and would easily anneal out below 600 °C. This argument gives rise to the alternative belief that a more stable V_{Zn}-defect complex is responsible for green emission.[60] Recently, Kuznetsov *et al.*[36] conducted PAS, PL, and Hall measurements on ZnO and related them to previous findings to ascertain the origins of green luminescence. It was concluded that an extrinsic acceptor-like impurity such as Cu_{Zn} was most likely responsible, and that these defect states could be readily passivated by V_O. As the formation energy of V_O is lower in reducing atmospheres, this alternative hypothesis could also explain the DLE trend observed here.

Despite these attempts to assign the green emission to particular defects, as of yet a direct method for detecting specific defects in ZnO does not currently exist, and so it cannot be demonstrated conclusively that V_{Zn}^{2-} are solely responsible for green emission. However, a large body of evidence supports the preferential formation of V_{Zn}^{2-} in O-rich conditions as we use, which also accounts for the highest green emission intensity for oxygen annealed ZnO. Therefore, we assign the green emission for these ZnO-nanorods to the presence of zinc vacancies.

C. ZnO-CuSCN device behaviour

The completed ZnO-nanorod/CuSCN device shown in Fig. 4(a) highlights the good pore-filling of CuSCN in the

nanorod array maximising the interfacial contact between the two semiconductors. The semi-log I-V plots for the ZnO-CuSCN p-n-heterostructure demonstrated (dark) rectifications of 3, 440, 600, and 21 500 at ±3 V for ZnO as-grown, and annealed in oxygen, nitrogen, and air atmospheres, respectively (Fig. 4(b)). The rectification value for
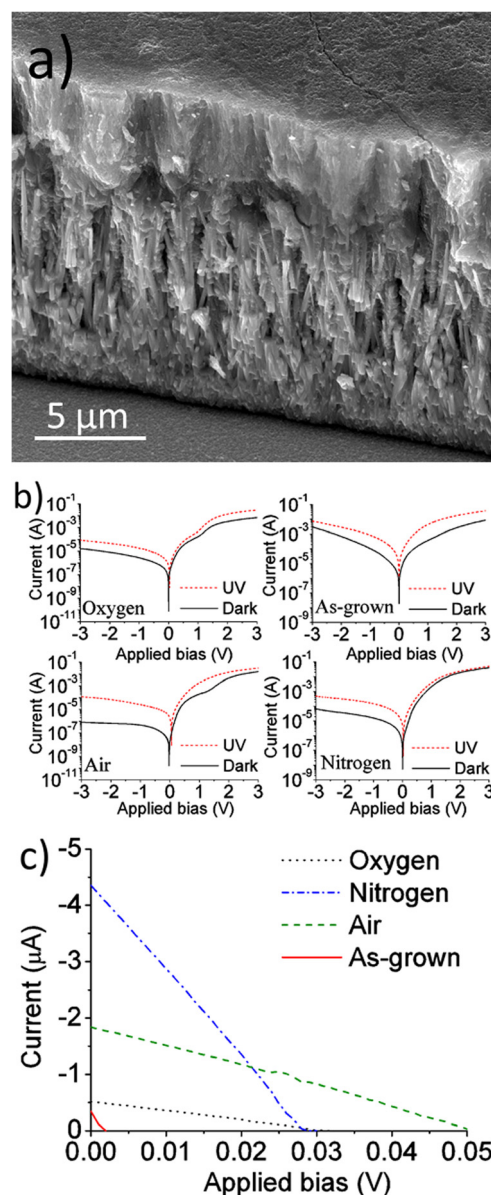

FIG. 4. (a) SEM micrograph cross-section of the completed ZnO-nanorod/CuSCN device, (b) semi-log I-V plots display the device rectification for each of the ZnO-nanorods used, and (c) enlarged I-V plot displaying the photovoltaic behaviour for each device under (380 nm, 0.8 mW cm⁻²) UV illumination.

air-annealed ZnO is at least two orders of magnitude greater than those previously reported for ZnO/CuSCN diodes.[61,62] The increased leakage current for oxygen/nitrogen-annealed ZnO is attributed to the surface defects formed during the anneal process; these act as recombination sites or trap states at the ZnO/CuSCN interface.

A photovoltaic effect was exhibited by the ZnO/CuSCN device under UV illumination, see Fig. 4(c). The photoconductive properties and wide band gap of both ZnO and CuSCN (3.6 eV) restrict the photo-excitation of electrons to a minimum energy of 3.3 eV and highlights the potential as a self-powered photodiode.

The photocurrent response of the devices operating at zero-bias increased with UV irradiances from 0.8 to 6.0 mW cm^{-2} and showed no sign of saturation or reduction (Fig. 5(a)). The nitrogen-annealed sample exhibited the highest photocurrent of ∼30 μA under 6 mW cm^{-2} UV irradiance. This is six times greater than the as-grown/oxygen annealed ZnO devices reported here, and at least twice the highest currently reported by Deng *et al.*, who tested using 8 W illumination.[42] Fig. 5(b) demonstrates the reliability of the devices with consistent and stable photocurrent after switching the UV light on and off six times. As discussed, although the measurement system was set to apply 0 V, a small dark current of −4 nA was detected, indicating a small applied-bias. When operating as a true self-powered photodetector, there would be no voltage source so the dark current would be zero. Extrapolating the photocurrent to true zero-bias would actually increase the photocurrent by ∼100%.

Response times were tested using a 532 nm pulsed laser that excited electrons via the 2.4 eV trap states to the ZnO E_C. The device exhibited a rapid τ_r of ∼25 ns (inset in Fig. 5(c)) and τ_f of ∼4 ms. We link the prolonged τ_f to intermediary trap states that prevent direct band-to-band

transition as shown by the diminished NBE and prominent DLE. Interestingly, the ZnO/CuSCN photodetector showed almost no response to the 3.5 eV (355 nm) pulsed laser. A similar device fabricated using pH 6 synthesised ZnO-nanorods shows a good photocurrent response to 355 nm pulse during the same experiment.[41] The nanorods grown at pH 11 (14 μm) reported here are much longer than those grown at pH 6 (2 μm), and additionally have a dense, compact layer at the base (closest to the FTO) approximately 4 μm thick. The absorption coefficient of ZnO at 355 nm is very high as it is well above the main band-edge absorption onset at ∼385 nm. Hence, when illuminated through the glass-FTO, as in the photo-response measurements, the majority of 355 nm photons will be absorbed close to the FTO. Due to the thick compact layer in the pH 11-grown rods, this absorption occurs well away from the junction, whereas for the pH 6-grown rods, which lack this thick layer, photons are absorbed closer to the junction. Due to internal recombination, only carriers excited near the junction region contribute to the photocurrent in the photodetector. Therefore, for the pH 11 rods grown here, 355 nm excitation does not create a significant photocurrent response, whereas 532 nm laser and 380 nm LED illumination that penetrate much further through the ZnO, do.

This photodetector is sensitive to specific ranges of UV 3.1-3.25 eV (380-400 nm) and blue-green 2.4 eV (475-525 nm) light. The responsivity of the device can be expressed as: $R_\lambda = \Delta I/(A \times P)$, where ΔI is the difference between illuminated and dark current, A is the contact area (0.1 cm^2), and P is the LED irradiance. Device responsivity peaks in the UV-region (380 nm), corresponding closely to the absorption peak for the ZnO/CuSCN heterostructure, see Fig. 5(d). The weak responsivity peak around 475-525 nm (Fig. 5(d)) and the absence of a visible-region absorption peak in the UV/vis
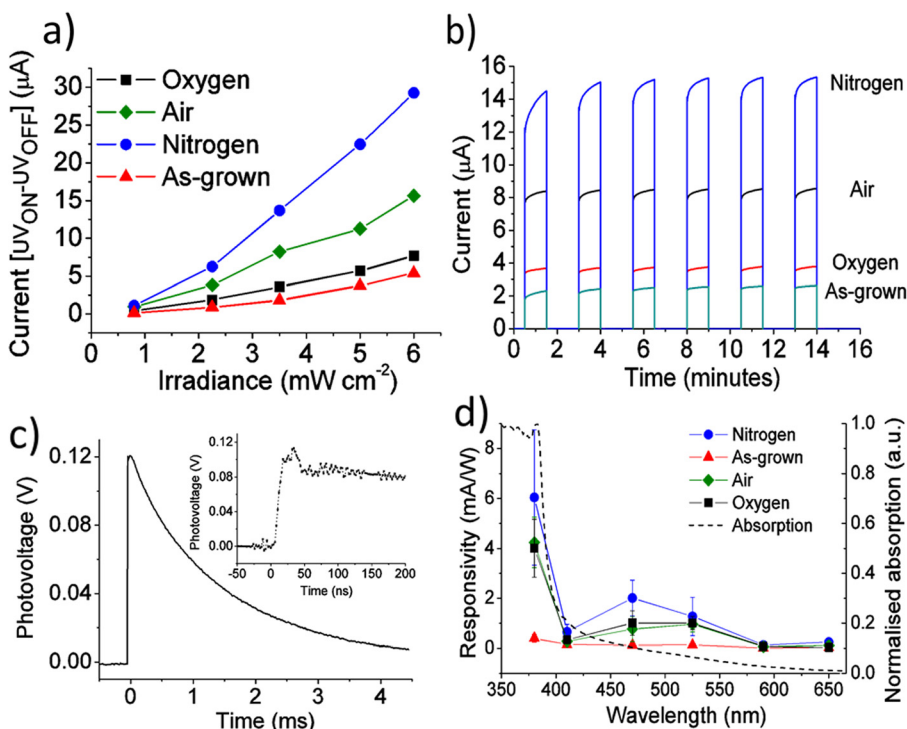

FIG. 5. (a) Photocurrent response of each ZnO-nanorod/CuSCN photodetector under increasing UV irradiances, (b) photocurrent stability under 380 nm, 3.5 mW cm^{-2} UV irradiance turned on (for 60 s) and off (for 90 s) six times, (c) fast transient photovoltage waveform in response to a 532 nm 5 ns-pulse with excitation energy of 0.1 mJ/pulse and enlarged rise time (inset), and (d) spectral responsivity (0.8 mW cm^{-2} irradiance) and the corresponding absorption spectra for the device.

spectra suggests the UV/vis illumination intensity is too low to excite carriers from the defect levels to the E_C. The maximum responsivity was calculated to be $0.05 \, A \, W^{-1}$ for 380 nm, 6 mW cm^{-2} irradiance at near-zero bias.

The difference in photocurrent response between the samples can be explained by the thermally induced defects. In the oxygen-annealed samples, V_{Zn}^{2-} act as electron trap states at the nanorod surface, and it is at this ZnO/CuSCN interface that the majority of carriers are photoexcited. When the electrons recombine with trap states, the carrier mobility is reduced and charge separation is hindered, reducing the photocurrent response. The high photocurrent measured for nitrogen-annealed ZnO may be attributed to the N-related shallow donor defects formed during the highly reducing nitrogen-anneal coupled with the absence of V_{Zn}^{2-} trap states. As the air-annealed sample lies between these two extremes, it follows that it would have an intermediate response, which correlates with the DLE in Fig. 3. The as-grown sample exhibits the lowest response of the fabricated devices due to the unreacted Zn-precursors trapped throughout the nanorod structure. These act as recombination sites that decrease both carrier mobility and concentration, and consequently have a negative effect on the device performance. However, the photocurrent of $\sim 5 \, \mu A$ at 6 mW cm^{-2} irradiance is comparable to those self-powered devices fabricated at higher temperatures.[28,38–41] This demonstrates the potential for flexible devices using as-produced ZnO material synthesised at temperatures $<100 \, °C$.

IV. CONCLUSIONS

N-doped ZnO nanorods were fabricated using an aqueous alkaline growth solution. Upon UV excitation, the nanorods exhibited strong green PL emission that was dependent on the annealing atmosphere. After reviewing the available theoretical and experimental analyses on this subject and relating this to our results, we infer that V_{Zn}-related defects are responsible for the observed green luminescence. Morphological and crystallographic changes to the nanorods occurred during the anneal process and were attributed to unreacted precursor material encapsulated near the nanorod surface. ZnO/CuSCN diodes were produced and tested as self-powered photodetectors. The results showed that the devices were sensitive in the UV and visible wavelengths with a maximum photocurrent response of $30 \, \mu A$ (at 6 mW cm^{-2} irradiance) for nitrogen-annealed nanorods. No additional encapsulation was required to stabilise the device or improve performance. We associate the performance characteristics to the high interfacial area provided by the nanorod array, good pore-filling of the CuSCN hole-collecting material, and N-related donor defects. Our devices show that it is possible to produce a self-powered flexible photodetector using a simple and inexpensive fabrication process.

ACKNOWLEDGMENTS

[1]G. Adamopoulos, A. Bashir, P. H. Wobkenberg, D. D. C. Bradley, and T. D. Anthopoulos, Appl. Phys. Lett. **95**, 133507 (2009).

[2]Y.-J. Lee, D. S. Ruby, D. W. Peters, B. B. McKenzie, and J. W. P. Hsu, Nano Lett. **8**, 1501 (2008).

[3]J. Shi, M. B. Starr, and X. Wang, Adv. Mater. **24**, 4683 (2012).

[4]J. Briscoe, E. Bilotti, and S. Dunn, Appl. Phys. Lett. **101**, 093902 (2012).

[5]J. Briscoe, M. Stewart, M. Vopson, M. Cain, P. M. Weaver, and S. Dunn, Adv. Energy Mater. **2**, 1261 (2012).

[6]M. Law, L. E. Greene, J. C. Johnson, R. Saykally, and P. D. Yang, Nature Mater. **4**, 455 (2005).

[7]H. D. Cho, A. S. Zakirov, S. U. Yuldashev, C. W. Ahn, Y. K. Yeo, and T. W. Kang, Nanotechnology **23**, 115401 (2012).

[8]S. Baruah and J. Dutta, Sci. Technol. Adv. Mater. **10**, 013001 (2009).

[9]M. N. R. Ashfold, R. P. Doherty, N. G. Ndifor-Angwafor, D. J. Riley, and Y. Sun, Thin Solid Films **515**, 8679 (2007).

[10]G. Amin, M. H. Asif, A. Zainelabdin, S. Zaman, O. Nur, and M. Willander, J. Nanomater. **2011**, 269692 (2011).

[11]L. Vayssieres, Adv. Mater. **15**, 464 (2003).

[12]Y. P. Sheng, Y. Jiang, X. Z. Lan, C. Wang, S. Y. Li, X. M. Liu, and H. H. Zhong, J. Nanomater. **2011**, 473629 (2011).

[13]Q. Li, V. Kumar, Y. Li, H. Zhang, T. J. Marks, and R. P. H. Chang, Chem. Mater. **17**, 1001 (2005).

[14]L. Lin, H. Watanabe, M. Fuji, T. Endo, S. Yamashita, and M. Takahashi, J. Am. Ceram. Soc. **92**, S165 (2009).

[15]L. E. Greene, M. Law, J. Goldberger, F. Kim, J. C. Johnson, Y. F. Zhang, R. J. Saykally, and P. D. Yang, Angew. Chem., Int. Ed. **42**, 3031 (2003).

[16]D. Li, Y. H. Leung, A. B. Djurisic, Z. T. Liu, M. H. Xie, S. L. Shi, S. J. Xu, and W. K. Chan, Appl. Phys. Lett. **85**, 1601 (2004).

[17]A. Janotti and C. G. Van de Walle, Rep. Prog. Phys. **72**, 126501 (2009).

[18]C.-C. Lin, S.-Y. Chen, S.-Y. Cheng, and H.-Y. Lee, Appl. Phys. Lett. **84**, 5040 (2004).

[19]M. Ding, D. Zhao, B. Yao, B. Li, Z. Zhang, and D. Shen, Appl. Phys. Lett. **98**, 062102 (2011).

[20]Q. X. Xia, K. S. Hui, K. N. Hui, D. H. Hwang, J. Singh, Y. R. Cho, S. K. Lee, W. Zhou, Z. P. Wan, C.-N. Ha Thuc, and Y. G. Son, Mater. Lett. **78**, 180 (2012).

[21]C. W. Zou, X. D. Yan, J. Han, R. Q. Chen, W. Gao, and J. Metson, Appl. Phys. Lett. **94**, 171903 (2009).

[22]C. L. Perkins, S.-H. Lee, X. Li, S. E. Asher, and T. J. Coutts, J. Appl. Phys. **97**, 034907 (2005).

[23]S. Limpijumnong, X. Li, S.-H. Wei, and S. B. Zhang, Appl. Phys. Lett. **86**, 211910 (2005).

[24]E. C. Lee, Y. S. Kim, Y. G. Jin, and K. J. Chang, Phys. Rev. B **64**, 085120 (2001).

[25]J. L. Lyons, A. Janotti, and C. G. Van de Walle, Appl. Phys. Lett. **95**, 252105 (2009).

[26]N. Bano, S. Zaman, A. Zainelabdin, S. Hussain, I. Hussain, O. Nur, and M. Willander, J. Appl. Phys. **108**, 043103 (2010).

[27]N. H. Alvi, M. Willander, and O. Nur, Superlattices Microstruct. **47**, 754 (2010).

[28]Z. Y. Zhan, L. X. Zheng, Y. Z. Pan, G. Z. Sun, and L. Li, J. Mater. Chem. **22**, 2589 (2012).

[29]J. Kramer, J. Appl. Phys. **47**, 1719 (1976).

[30]C. Ton-That, L. Weston, and M. Phillips, Phys. Rev. B **86**, 115205 (2012).

[31]K. H. Tam, C. K. Cheung, Y. H. Leung, A. B. Djurisic, C. C. Ling, C. D. Beling, S. Fung, W. M. Kwok, W. K. Chan, D. L. Phillips, L. Ding, and W. K. Ge, J. Phys. Chem. B **110**, 20865 (2006).

[32]A. B. Djurišić, W. C. H. Choy, V. A. L. Roy, Y. H. Leung, C. Y. Kwong, K. W. Cheah, T. K. G. Rao, W. K. Chan, H. F. Lui, and C. Surya, Adv. Funct. Mater. **14**, 856 (2004).

[33]H. Zhou, H. Alves, D. M. Hofmann, W. Kriegseis, B. K. Meyer, G. Kaczmarczyk, and A. Hoffmann, Appl. Phys. Lett. **80**, 210 (2002).

[34]Y.-J. Lin, C.-L. Tsai, Y.-M. Lu, and C.-J. Liu, J. Appl. Phys. **99**, 093501 (2006).

[35]X. L. Wu, G. G. Siu, C. L. Fu, and H. C. Ong, Appl. Phys. Lett. **78**, 2285 (2001).

[36]K. Knutsen, A. Galeckas, A. Zubiaga, F. Tuomisto, G. Farlow, B. Svensson, and A. Kuznetsov, Phys. Rev. B **86**, 121203 (2012).

[37]Y. B. Zhang, G. K. L. Goh, K. F. Ooi, and S. Tripathy, J. Appl. Phys. **108**, 083716 (2010).

[38]W. Jin, Y. Ye, L. Gan, B. Yu, P. Wu, Y. Dai, H. Meng, X. Guo, and L. Dai, J. Mater. Chem. **22**, 2863 (2012).

[39]Q. Yang, Y. Liu, Z. T. Li, Z. Y. Yang, X. Wang, and Z. L. Wang, Angew. Chem., Int. Ed. **51**, 6443 (2012).

[40]X. Li, C. Gao, H. Duan, B. Lu, Y. Wang, L. Chen, Z. Zhang, X. Pan, and E. Xie, "High-performance photoelectrochemical-type self-powered UV photodetector using epitaxial TiO2/SnO2 branched heterojunction nano-structure," Small (to be published).

[41]S. M. Hatch, J. Briscoe, and S. Dunn, Adv. Mater. **25**, 867 (2013).

[42]S. X. Yang, J. Gong, and Y. L. Deng, J. Mater. Chem. **22**, 13899 (2012).

[43]K. M. McPeak, T. P. Le, N. G. Britton, Z. S. Nickolov, Y. A. Elabd, and J. B. Baxter, Langmuir **27**, 3672 (2011).

[44]L. E. Greene, B. D. Yuhas, M. Law, D. Zitoun, and P. Yang, Inorg. Chem. **45**, 7535 (2006).

[45]J. Joo, B. Y. Chow, M. Prakash, E. S. Boyden, and J. M. Jacobson, Nature Mater. **10**, 596 (2011).

[46]S. M. Hatch, J. Briscoe, and S. Dunn, Thin Solid Films **531**, 404 (2013).

[47]A. Kaschner, U. Haboeck, M. Strassburg, G. Kaczmarczyk, A. Hoffmann, C. Thomsen, A. Zeuner, H. R. Alves, D. M. Hofmann, and B. K. Meyer, Appl. Phys. Lett. **80**, 1909 (2002).

[48]L. E. Halliburton, N. C. Giles, N. Y. Garces, M. Luo, C. C. Xu, L. H. Bai, and L. A. Boatner, Appl. Phys. Lett. **87**, 172108 (2005).

[49]H. Q. Wang, G. Z. Wang, L. C. Jia, C. J. Tang, and G. H. Li, J. Phys. D: Appl. Phys. **40**, 6549 (2007).

[50]A. Janotti and C. G. Van de Walle, Phys. Rev. B **76**, 045501 (2007).

[51]A. F. Kohan, G. Ceder, D. Morgan, and C. G. Van de Walle, Phys. Rev. B **61**, 15019 (2000).

[52]S. Zhang, S.-H. Wei, and A. Zunger, Phys. Rev. B **63**, 075205 (2001).

[53]F. Oba, S. R. Nishitani, S. Isotani, H. Adachi, and I. Tanaka, J. Appl. Phys. **90**, 824 (2001).

[54]D. Look, G. Farlow, P. Reunchan, S. Limpijumnong, S. Zhang, and K. Nordlund, Phys. Rev. Lett. **95**, 225502 (2005).

[55]K. Vanheusden, W. L. Warren, C. H. Seager, D. R. Tallant, J. A. Voigt, and B. E. Gnade, J. Appl. Phys. **79**, 7983 (1996).

[56]C. Patterson, Phys. Rev. B **74**, 144432 (2006).

[57]C. G. Van de Walle, Phys. Rev. Lett. **85**, 1012 (2000).

[58]G. A. Shi, M. Stavola, S. J. Pearton, M. Thieme, E. V. Lavrov, and J. Weber, Phys. Rev. B **72**, 195211 (2005).

[59]M. D. McCluskey and S. J. Jokela, J. Appl. Phys. **106**, 071101 (2009).

[60]A. B. Djurišić, Y. H. Leung, K. H. Tam, Y. F. Hsu, L. Ding, W. K. Ge, Y. C. Zhong, K. S. Wong, W. K. Chan, H. L. Tam, K. W. Cheah, W. M. Kwok, and D. L. Phillips, Nanotechnology **18**, 095702 (2007).

[61]W. B. Wu, S. G. Cui, C. H. Yang, G. D. Hu, and H. T. Wu, Electrochem. Commun. **11**, 1736 (2009).

[62]Q. B. Zhang, H. H. Guo, Z. F. Feng, L. L. Lin, J. Z. Zhou, and Z. H. Lin, Electrochim. Acta **55**, 4889 (2010).

[63]See supplementary material at http://dx.doi.org/10.1063/1.4805349 for graphical representation of the Gaussian fits presented in Table I.